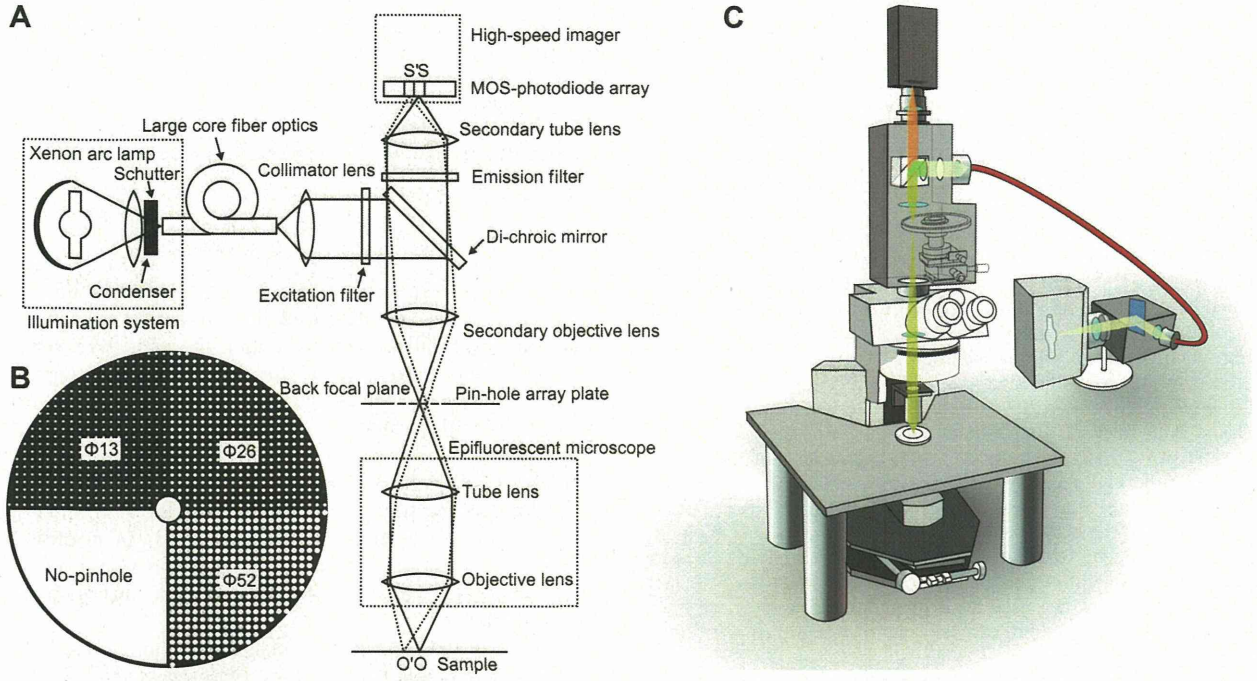

Fig. 1. Optical configuration of the nonscanning confocal microscope. *A*: schematic of the new confocal microscope. The confocal epifluorescent optics were designed to fit a conventional upright microscope with an objective lens and a tube lens (surrounded by dashed line). A pinhole array was positioned at the back focal plane, on which epifluorescent optics were placed. These optics consist of a secondary objective lens and secondary tube lens, between which a mirror unit (excitation filter, dichroic filter, and emission filter) was inserted. The fluorescence was then projected onto a complementary metal-oxide semiconductor (CMOS) high-speed imager. Lights from a sample in objective plane (O and O′) correspond to lights sampled by photodiodes (S and S′). *B*: schematic drawing of the pinhole array plate consisting of 4 sectors with different pinhole patterns [pinhole diameters (Φ) of 13, 26, or 52 μm and a no-pinhole sector]. *C*: illustration of the new confocal microscopy module attached to a conventional upright microscope (BX51WI; Olympus). A microscope was placed on a movable table combined with fixed table. The confocal module was placed on the upper optical port of the microscope. The excitation light was introduced by a large core fiber optic cable attached to a xenon light source with an electrical shutter.

secondary objective lens (f = 90 mm) and then projected onto each corresponding photodiode (S and S′) of the CMOS-photodiode array after traveling through a secondary tube lens (f = 90 mm; XLFuor2X; Olympus) and a mirror unit containing a dichroic mirror and emission filter. The secondary objective lens and the secondary tube lens were at onefold magnification. The optics was adjusted for the ×20 objective lens (×20/0.95 or ×20/1.0; Olympus), and the resulting field of view was approximately 500 × 500 μm. An overview of the microscope is shown in Fig. 1*C*.

Pinhole array. Our pinhole array (Fig. 1*B*) was made, from the type of glass plates used in the commercial disk confocal unit (DSU; Olympus), by a chromium deposition technique. The disk was divided into four sectors. Three of the sectors contained pinholes with 13-, 26-, or 50-μm diameters. The fourth sector did not have any chromium deposition. The glass plate (disk) was fixed on a rotary shaft and mounted on an x–y translation table (Sigma Koki, Tokyo, Japan), and the rotation angle was adjusted (θ adjustment) to align each pinhole with its corresponding pixel of the imager.

The diameters of the pinholes were chosen to match the size of the first minimum of the Airy disk as follows:

$$\Phi = 1.22 \times \lambda / \mathrm{NA}, \quad (1)$$

where λ is the wavelength of the excitation light (0.53 μm: excitation light for di-4-ANEPPS) and NA equals the ratio of NA (1.0) and magnification (×20) of the objective lens. According to *Eq. 1*, the calculated Φ was 12.9 μm.

To compensate for the loss of light transmission through the 13-μm pinholes, we also used larger pinholes. This was accomplished by dividing the disk into four sectors: one without pinholes and three covered with a grid pattern of pinholes (13, 26, or 52 μm in diameter) arranged in a square grid with an interval of 100-μm distance. The center part, 1 × 1 cm that contains 10^4 pinholes in a sector, was used as a pinhole array.

Slice preparation and staining with VSD. All animal experiments were performed according to protocols approved by the Animal Care and Use Committee of Tokushima Bunri University. Hippocampal slices were prepared from 4- to 5-wk-old male rats decapitated under deep isoflurane anesthesia after perfusion with ice-cold artificial cerebrospinal fluid (aCSF; 124 mM NaCl, 2.5 mM KCl, 2 mM $CaCl_2$, 2 mM $MgSO_4$, 1.25 mM NaH_2PO_4, 26 mM $NaHCO_3$, and 10 mM glucose; pH 7.4) bubbled with 95/5% O_2/CO_2 gas. The brains were quickly removed and cooled in aCSF. After cooling for 5 min, the hippocampus and the surrounding cortex was dissected and sliced into 400-μm transverse sections using a vibratome (Leica VT1000). Following incubation in gassed aCSF for 3–5 min, each slice was transferred onto a fine-mesh membrane filter (Omnipore Membrane Filter, JHWP01300; Millipore) held in place by a thin Plexiglas ring (inner diameter, 11 mm; outer diameter, 15 mm; thickness, 1–2 mm). These slices were transferred to a moist chamber continuously supplied with a humidified O_2-CO_2 gas mixture. The temperature was held at 32°C for 1 h and then maintained at room temperature thereafter.

Bulk staining and imaging with the VSD. After the 1-h incubation, each slice was stained for 25 min with 100 μl of the VSD solution, containing 0.2 mM di-4-ANEPPS (Molecular Probes) in 2.5% ethanol, 0.13% Cremophor EL (Sigma), 1.17% distilled water, 48.1% fetal bovine serum (Sigma), and 48.1% aCSF. After washing, sections were incubated at room temperature for ≥1 h before they were imaged.

Single-cell staining and imaging with the VSD. Individual pyramidal cells in the CA1 area of the sections were visualized using a conventional CMOS camera (SKDCE-2EX; Sigma Koki) with oblique illumination. Patch-clamp recordings, in whole cell mode, were made

using a patch-clamp amplifier with a capacitive headstage (Axoclamp 700B; Axon Instruments, Foster City, CA). Borosilicate glass pipettes (Sutter Instruments, Novato, CA) were pulled using a P-97 Flaming/Brown pipette puller (Sutter Instruments). The cesium-based pipette internal solution, used for whole cell voltage-clamp experiments, consisted of (in mM): 120 $CsMeSO_3$, 10 HEPES, 4 $MgCl_2$, 4 NaATP, 0.4 NaGTP, 10 Na-phosphocreatine, 5 QX-314, 10 EGTA; pH was adjusted to 7.2 (2–4 MΩ). Whole cell recordings were low-pass filtered at 3 kHz and digitized at 10 kHz (ITC-18; InstruTECH). Data were fed into a computer for online and offline analysis using laboratory-developed software on IGOR Pro (WaveMetrics). In voltage-clamp mode, a test membrane potential step (−10 mV) was always applied before electrical stimulation, and traces with series resistance (R_s) <20 MΩ were accepted. After establishing optimal whole cell clamp conditions, the internal solution of the patch pipette was replaced with internal solution containing VSD (1 mg di-2-ANEPPS/1 ml internal solution) for 20–30 min. The internal solution was then replaced with internal patch pipette solution. For the patch pipette perfusion, we used a pipette holder with perfusion port and suction port. Thin-tipped polypropylene tubing was inserted into the perfusion port and connected to a syringe. The tip of the perfusion tube was positioned 400–600 μm from the tip of the patch pipette. The internal pipette solution was replaced by applying pressure through the syringe after making the whole cell condition.

For VSD imaging, we used a mirror unit consisting of a 530- ± 15-nm excitation filter, a 590-nm dichroic mirror, and 610- ± 20-nm emission filter.

Staining and imaging with Ca^{2+} indicator. Fifty micrograms of Oregon Green 488 BAPTA-1, AM (special package; Molecular Probes) was dissolved into 10 μl of 0.5% Cremophor EL-DMSO mixture and added to 2-ml aCSF to yield final concentrations of 0.0025% (20 mM) AM-ester dye, 0.002% Cremophor EL, and 0.5% DMSO. Slices were bath-stained for 40 min at 37°C with an aliquot (100 μl per section) of the Ca^{2+} indicator solution. Sections were washed and incubated at room temperature for ≥1 h before imaging.

For imaging of the Ca^{2+} indicator, we used a mirror unit for FITC (FITC-3540B, BrightLine series; Semrock) consisting of a 482- ± 17-nm excitation filter, a 513-nm dichroic mirror, and a 536- ± 20-nm emission filter.

RESULTS

Optical sectioning. To test the optical sectioning of the new confocal module, we measured light intensity reflected on a total reflection mirror placed under the objective lens and plotted the light intensity at the center of the imager as a function of focus height along the *z*-axis (Fig. 2*A*). When in the no-pinhole configuration (Fig. 1*B*, No-pinhole), the microscope worked as a conventional bright-field microscope. The intensity of the reflected light linearly decreased around the focal plane as the focus was raised along the *z*-axis, as determined under transmitted light illumination. In contrast, the pinhole configurations (diameters: 13 μm on *sector 1*, 26 μm on *2*, and 53 μm on *3*) resulted in peak light intensity around the focus plane.

Next, we tested the microscope using a calibration kit of fluorescent bead preparation [Rainbow Fluorescent Particle Slide 6 Sizes (0.56, 0.96, 3.0, 5.5, 10.0, and 15.5 μm), FPS-M57-6; Spherotech]. We used particle size 5.5 for the calibration. Figure 2*B* shows a composed (slit) image consisting of a line

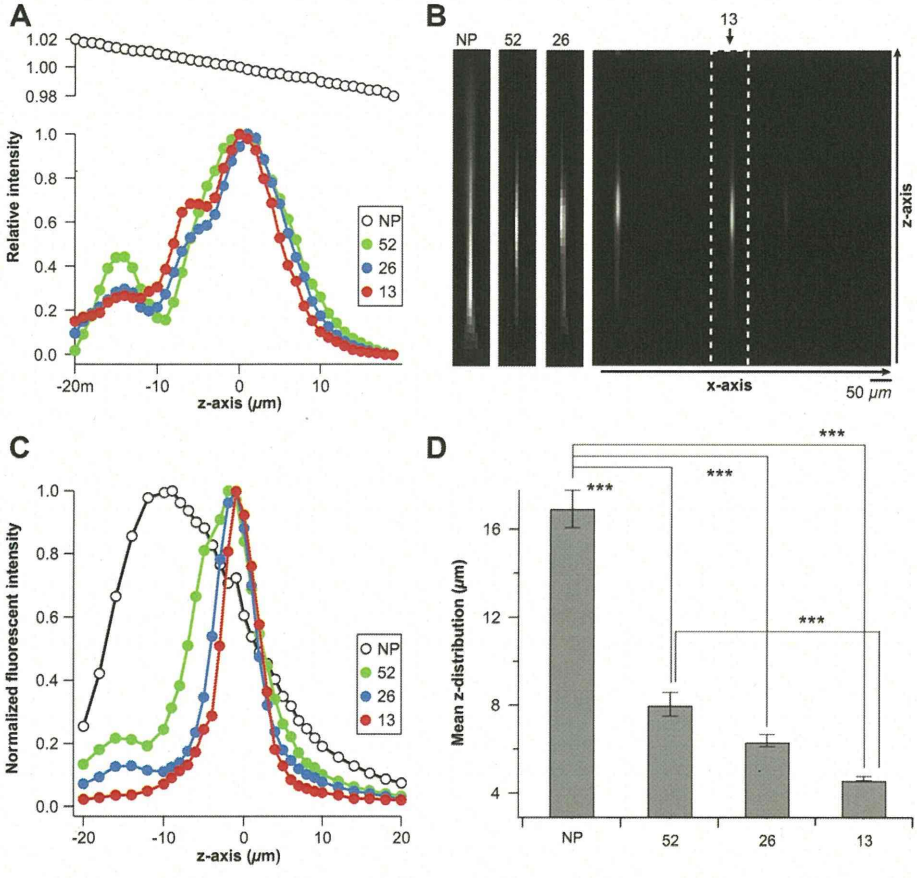

Fig. 2. Basic optical characteristics of the new confocal microscopy module. *A*: light intensity detected at the imager after reflection from a total reflection mirror placed under an objective lens in the nonpinhole configuration (NP; open circles) and with arrays of pinholes of 13-μm (13; red), 26-μm (26; blue), and 52-μm (52; green) diameter. On the *z*-axis, 0 indicates the focal point determined with transmitted light. *B*: fluorescent images of the standard fluorescent bead preparation, swept by a single horizontal line of the imager, collected using the no-pinhole, 52, 26, and 13 configurations. *C*: the profile of fluorescence intensity of beads shown in *B* for the no-pinhole and 52-, 26-, and 13-μm pinhole configurations. *D*: pooled data of the half-length of the profile shown in *C*. ***$P < 0.001$, Tukey post hoc test.

of pixels collected from different focal planes (1-μm step, 40 steps). Figure 2*B*, 13, shows a slit image taken when the 13-μm pinhole array was used. Here, 2 or 3 lines are observed along the *z*-axis, each reflecting an image of a bead. The same image, indicated by dashed line, was taken with the 26-μm (Fig. 2*B*, 26) and 52-μm (Fig. 2*B*, 52) pinhole arrays. Finally, an image of the same bead, taken using no-pinhole configuration (*sector 0*), is shown in Fig. 2*B*, NP. The changes in light intensities along a line and within the same pixel are plotted in Fig. 2*C*. The mean *z*-distribution was measured as the half-width of the fluorescence intensity profiles along the *z*-axis, recorded for 20 different beads. These data are shown in Fig. 2*D*. The half-width was significantly decreased when pinholes were used, and the size of pinhole inversely affected the *z*-resolution of the beads. The results indicate that the configuration used in this study effectively improved depth resolution even when the largest pinholes were used.

Images and noise consideration. Fluorescent images of VSD-stained hippocampal slices were obtained with the confocal module using all four pinhole configurations (no-pinhole and diameters equal to 52, 26, and 13 μm). The intensity of fluorescence at each pixel decreased as the size of the pinhole decreased; that must be proportional to the fourth power of the pinhole radius. To acquire images within the dynamic range of the imager, the images were acquired at four different accumulation times (0.1, 1, 10, and 100 ms per frame). The consecutive images were obtained at different focal depths in 5-μm steps.

The images obtained with the 13-μm pinhole array had the finest resolution, and the images tended to blur as the diameter of the pinholes increased. The images obtained with the 13-μm pinhole appeared different at every 5-μm step along the *z*-axis, whereas images taken without pinholes looked similar across the 30-μm change in the *z*-axis. The time courses of the optical signal obtained with these conditions are presented on the right-hand side of the images of Fig. 3*A*. Image intensities decreased and baseline-normalized noise increased as pinholes became finer (Fig. 3*A*).

To identify the source of the noise in the optical signals, the standard deviation of the noise [i.e., root-mean-square (RMS) noise] was measured in pixels from images obtained using different acquisition conditions [e.g., acquisition rates ranging from 0.1 to 200 ms and presence or absence of a neutral density (ND) filter]. To sample a range of fluorescence intensities, a vertical line of pixels through the center of the images was used for this calculation and was plotted on the same graph as shown in Fig. 3*B*. The RMS noise increased as the fluorescence increased for each pinhole configuration. A double-logarithmic plot of this relationship shows that normalized RMS noise by F_0 (RMS noise/F_0) decreased as a first order function of F_0 below an F_0 equivalent to 1% saturation of imager (approximately 1×10^6 electrons) and decreased proportionally to the square root of F_0 when F_0 was >1%. That is, when F_0 was <1% of the maxima of imager photodetector, the major cause of the noise was equal to the constant amount of noise (~0.02%, corresponding to 230 electrons) for the imaging device (Dr. Michinori Ichikawa, BrainVision, personal communication). In contrast, when F_0 was >1%, the major source of noise was the shot noise, which is proportional to square root of light intensity.

VSD signals obtained from a hippocampal slice. Figure 4, *A* and *B*, compares the VSD signals in the CA1 area of hippocampal slices on electrical stimulation of the Schaffer collateral pathway. The *top* shows the data acquired in the no-pinhole configuration, and the *bottom* shows the data acquired using the 52-μm pinhole array. Both signals were acquired at a frame rate of 0.3 ms per frame. The intensity of the initial fluorescence with the two conditions was matched by applying a ND filter (6% transmission) to the no-pinhole condition. The optical signal, normalized by initial fluorescence, was almost identical in both the nonpinhole and 52-μm pinhole condition. The optical signal of representative pixels, along the axis parallel to pyramidal cells, is shown in Fig. 4*C* for the nonpinhole (*A*) and 52-μm pinhole (*B*) configurations. As indicated by the superimposed traces, the signals obtained from both configurations were nearly the same.

Figure 4*D* shows a confocal fluorescent image of a pyramidal cell, perfused with VSD (di-2-ANEPPS), from a whole cell clamp preparation collected at a frame rate of 10 ms per frame using the 52-μm pinhole array. The sensitivity of the optical signal was about 10%/100-mV change (Fig. 4*E*), similar to the value previously reported for di-4-ANEPPS (Loew et al. 1992). Figure 4 shows representative images of the optical signals detected for membrane potentials of −20, 20, −50, and 50 mV.

Ca^{2+} imaging. Figure 5*A* shows the optical signal acquired from CA1 area of a hippocampal slice being loaded with Oregon Green 488 BAPTA-1, AM. The data presented here were acquired at a frame rate of 5 ms per frame using the 52-μm pinhole array and show the response of the CA1 area on electrical stimulation of the Schaffer collateral pathway. The data show several cells in the pyramidal cell layers that exhibited large changes in fluorescence on stimulation, whereas the responses were less conspicuous in the stratum radiatum. It is also interesting to note that the initial fluorescence levels were high in s. alveus, and the responses remained obvious in this region (Fig. 5, *A* and *B*). Figure 5*C* shows the peak optical signals for each pixel. The large, steep response shown in the upper right corner represents the Ca^{2+} response in a single cell, corresponding to the optical signal represented in Fig. 5*B*, *trace 4*.

The 26-μm pinhole array was also effective at detecting the response of these cells when acquired at 10 ms per frame, but the data were similar to those presented here. In the nonpinhole condition, it was difficult to see the specimen as the images were blurred.

Fig. 3. Fluorescent images of rat hippocampal slices stained with voltage-sensitive dye (VSD) and acquired by the confocal microscopy module using different pinhole figurations. *A*: images of VSD-stained hippocampal slice collected using the different pinhole configurations at different positions in the *z*-axis. The *right* traces show the optical signal from a single pixel of the image. *B*: root-mean-square (RMS) noise in the time course of the fluorescence plotted against initial fluorescent intensity (F_0). Fluorescent intensity was expressed relative to the saturation level of imager (approximately 1 M electron per pixel). RMS noise was calculated as a sum of square roots of measurements at time *t* (F_t) deviation from the F_0 (i.e., the standard deviation of the optical signal). The measurements plotted in the graph were obtained with different pinhole conditions (black, no-pinhole; blue, 13 μm; green, 26 μm; red, 52 μm) at acquisition rates ranging from 0.1 to 200 ms for different pixels in the view. *C*: normalized RMS noise ($\Delta F/F_0$) plotted against F_0 in double-logarithmic scale for the same measurements as *B*. The black line shows the constant RMS value of 0.02% obtained from the darkest RMS noise divided by F so that the slope of the line (a constant/F) on the graph equals to −1.0. The red line shows the slope of photon shot noise proportional to square root of F_0.

DISCUSSION

Advantages and limitation of the system. Using a fixed-pinhole array, our confocal module achieves confocal signals (Amos and White 2003; Pawley 2006) at all of the 10,000 pixels on an imager simultaneously. Because the pinholes are stationary, there is no scanning noise (Saggau 2006) as seen in traditional confocal microscopy such as confocal laser-scanning microscopes (CLSM) and Nipkow disk confocal microscopes (Kino 1995). In addition, because the image acquisition rate is not restricted by a scanning mechanism, our system can

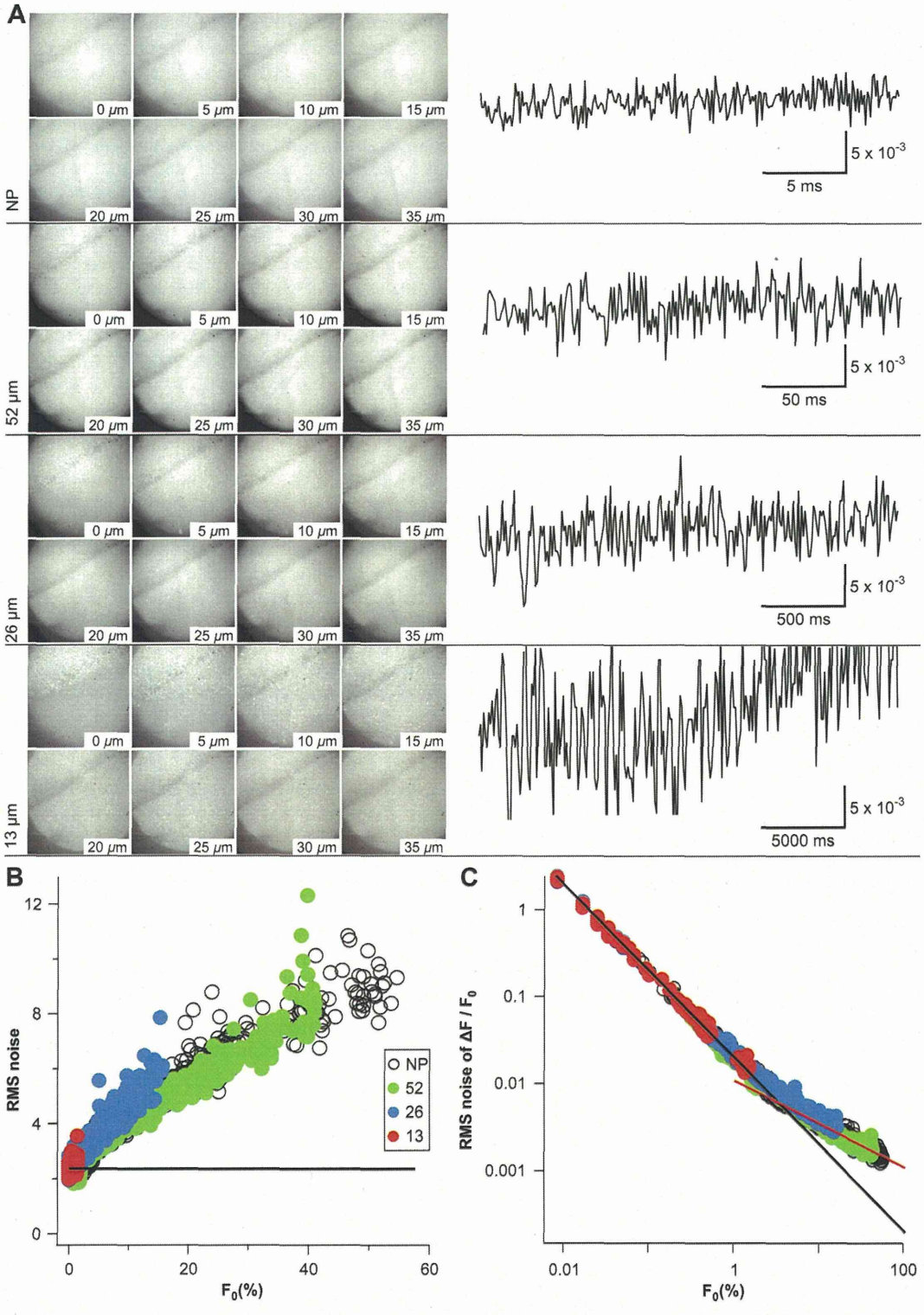

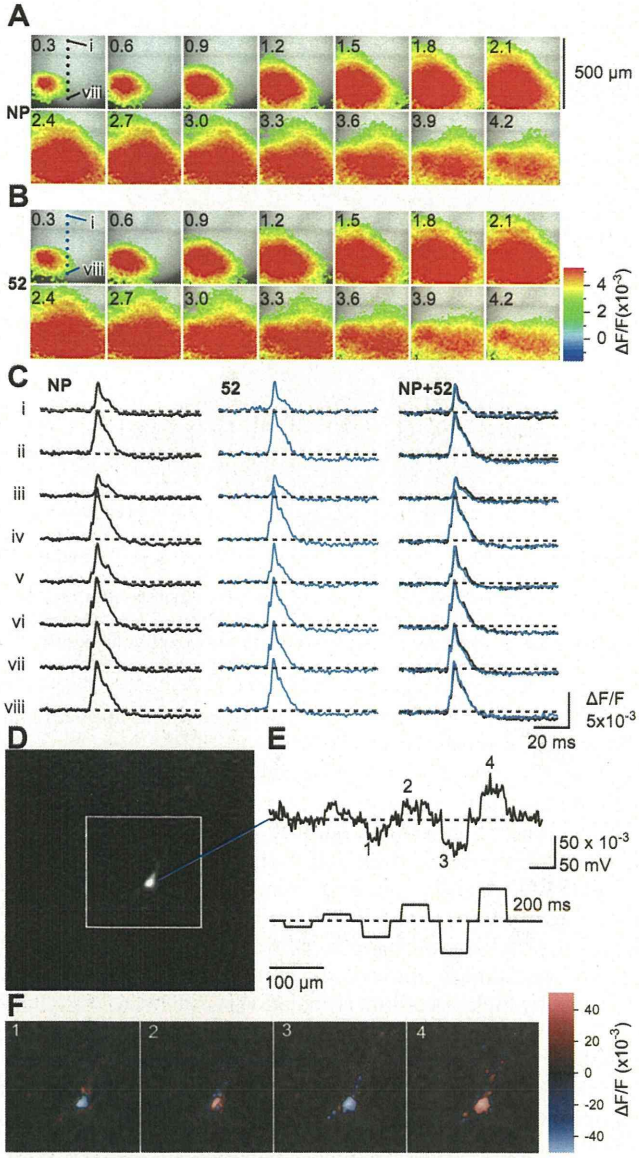

Fig. 4. Representative optical signals recorded from VSD-stained hippocampal slices on an electrical stimulation of the Shaffer collateral pathway using the conventional (no-pinhole) and 52-μm pinhole configurations. Consecutive images are of fluorescence change ($\Delta F/F$), in pseudocolor, recorded after electrical stimulation to Schaffer collateral pathway using the no-pinhole (*A*) and 52-μm diameter (*B*) pinhole configurations at the frame rate of 0.3 ms per frame. The number of each image is the time after an electrical stimulation given to the Schaffer collateral (0 ms). The initial fluorescence was matched by using a neutral density filter (6%) when no pinhole was used. *C*: optical traces of the pixels indicated in *A* and *B* (*i–viii*) in no-pinhole condition and 52-μm pinhole condition. Superimposed traces are shown in NP+52. *D*: fluorescent image of VSD-stained pyramidal cell in the CA1 area. The images were taken at the frame rate of 10 ms per frame when 52-μm pinhole configuration was used. *E*: optical traces under voltage-clamp condition at the center of the cell are shown on the right-hand side of the images. *F*: images of the fluorescent change in pseudocolor code at the acquisition times indicated in the *E* traces. One corresponds to −20-mV, 2 to 20-mV, 3 to −50-mV, and 4 to 50-mV membrane potential.

achieve higher acquisition rates, which are limited only by the imaging system. In its implementation, the system has a spatial resolution of only 100 × 100 pixels. The use of more dense pinholes and a camera with a larger number of pixels can decrease pixilation. As in normal wide-field epifluorescence microscopes, it is not very straight-forward to achieve very high excitation light densities. Moreover, only a small fraction of the light that is projected from the light source onto the pinhole array passes the pinholes (1.3, 4.6, and 18.4% of the illuminated area for 13-, 26-, and 52-μm pinholes, respectively). Use of a more intense light source will increase effective excitation intensities and, hence, SNR.

Comparison with other high-speed imaging systems. For the CLSM, the product of frame rate and number of pixels is limited by the speed of the scanning process such that frame rates >50 Hz demand for a strict reduction of the number of measurement points. For off-the-shelf disk-scanning confocal system, the temporal resolution is often limited by the imager, and there are similar tradeoffs between the spatial resolution and frame rates. Confocal spot detection can avoid this tradeoff and has been used to visualize Ca^{2+} microdomain dynamics (Escobar et al. 1994; DiFranco et al. 2012; DiGregorio et al. 1999). This method has the clear advantage of measuring the optical signal from a single point at high speed with good SNR (Bradley et al. 2009; Fink et al. 2012). Moreover, recent optoacoustic device-driven random-access fluorescence microscopy (Bullen and Saggau 1999; Otsu et al. 2008; Saggau et al. 1998), which enables the measurement of several points, has the advantage that it can measure several points with a performance similar to the single-point measurements. These measurements can then be converted into a multiphoton depth image (Duemani Reddy et al. 2008). The nonlinear measurements, using multiphoton microscopy, were extended to record second harmonic generation signals (Dombeck et al. 2004, 2005; Nuriya et al. 2006).

The light-sheet microscopy, with special focus on high-speed image acquisition such as the selective plane illumination microscopy (SPIM; Huisken 2012; Huisken and Stainier 2009) and/or the objective-coupled planar illumination (OCPI) microscope (Turaga and Holy 2012) can provide high-speed image acquisition while still allowing the thinner optical dissection and volumetric imaging. With these techniques, the image acquisition speed is determined by the imager acquisition rate rather than the scanning devices, similar to the present system. Moreover, because SPIM and OCPI focus excitation light using a thin sheet, often through a cylindrical lens, they offer advantages in terms of excitation light intensity compared with our system.

Light-sheet microscopy has been used mostly for the imaging of clear objects, such as embryos, because other specimens produce shadows that interfere with visualization. Recent introduction of multidirectional SPIM (mSPIM; Huisken and Stainier 2007) is overcoming this problem. In addition, the spatial resolution has now been improved by using nonlinear excitation with stimulated emission depletion (STED; Friedrich et al. 2011).

Compared with these examples of high-speed imaging microscopy, the current system has a clear disadvantage in terms of excitation light intensity. However, the simple configuration of our module offers an inexpensive high-speed imaging option for users that require a wider field of view such as that required for functional neuronal circuit imaging. In this regard, the module shares many of the advantages of confocal spot detection and fast frame acquisition of SPIM. Adding to this advan-

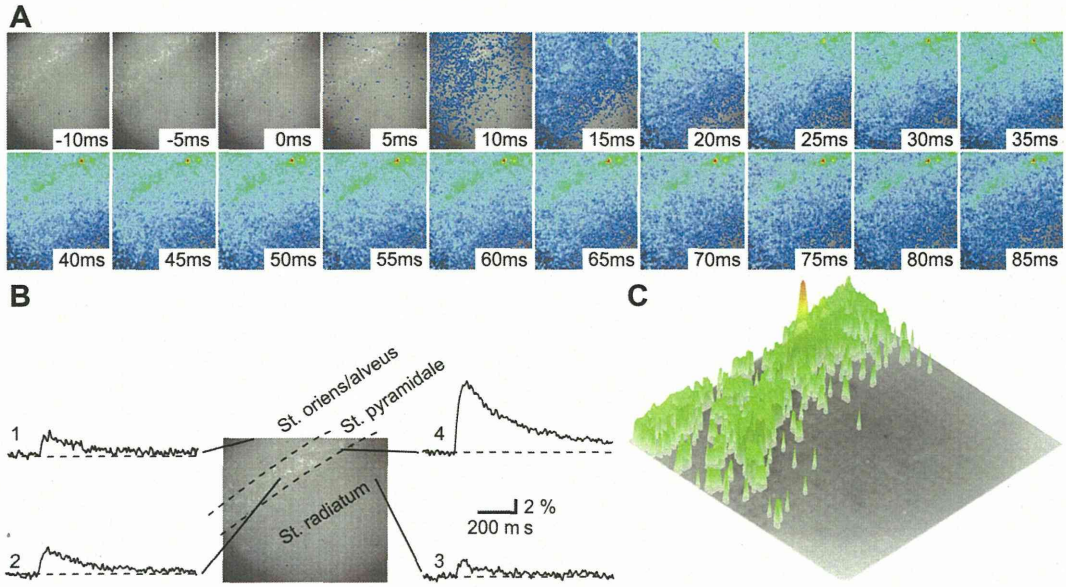

Fig. 5. Fluorescent Ca^{2+} imaging of indicator-stained hippocampal slices. *A*: consecutive images showing the spread of Ca^{2+} in response to an electrical stimulation (0 ms) of the Schaffer collateral. *B*: the Ca^{2+} signal at 4 representative pixels in the image. Shown are 1 for stratum oriens/alveus, 2 for s. pyramidale, 3 for s. radiatum, and 4 for a cell showing huge Ca^{2+} change. *C*: the 3-dimensional representation of the peak signal measured in each pixel. A highest spot is seen in a cell body of a neuron corresponding to 4 in *B*. The images were taken using the 26-μm pinhole configuration at a frame rate of 5 ms per frame.

tage, oblique illumination with a separate optical axis could be useful, especially for low-magnification wide-field optical recording.

Light sources. For single-point measurements, CLSM can use lasers as light source. Because CLSM offers flexibility in choice of power and range of excitation wavelengths, these microscopes can achieve high SNR. However, stability of the laser and speckle noise caused by its coherent nature can also cause noise. In contrast, pinhole-array confocal microscopy requires a wide field of illumination. Here, lasers are less suitable due to their narrow beam diameter. Instead, excitation light is typically supplied by a xenon arc lamp, halogen light, or high-power LED with temperature compensation (Nishimura et al. 2006) because of their wider area of illumination. These are stable and inexpensive, but the light intensity is relatively limited, rendering them less suitable for point-scanning applications. Fortunately, rapid progress in high-power LED technology could overcome this limitation.

Usefulness in VSD and Ca^{2+} imaging. Among the various imaging techniques, techniques based on a fast VSD (Cohen et al. 1974; Salzberg et al. 1973) offer high spatial and temporal resolution. VSD rapidly converts changes in the membrane potential, such as action potentials, into optical signals using changes in either the absorption of transmitted light or emission of fluorescence (Cohen et al. 1978; Grinvald et al. 1988; Grinvald and Hildesheim 2004; Peterka et al. 2011). Recent progress in imaging devices together with the speed of the VSD response have allowed us to follow the submillisecond time scale of neuronal activities by VSD imaging. However, because the fractional optical signal is small, the difficulty in obtaining a good SNR is the most critical. Efforts have been aimed at improving the SNR by increasing the photon efficacy of wide-field excitation optics to increase the fluorescence intensity and achieve rapid image acquisition (Ratzlaff and Grinvald 1991; Tominaga et al. 2000).

The magnitude of the signal we obtained from hippocampal slices bulk-stained with VSD (di-4-ANEPPS) was approximately 4×10^{-3}. This is far smaller than the VSD signal expected (a relative change of few percent per 100 mV) from a single plasma membrane because of the absence of nonresponsive fluorescence background (Loew et al. 1992). In addition, VSD signals obtained from the CA1 area showed maximum response on Schaffer collateral stimulation in the layer of s. radiatum. However, as we have shown earlier, the signal was almost uniform if the membrane potential was elevated by high-potassium stimulation when the action potential was inhibited by TTX (Tominaga et al. 2009). These problems are related to the fact that the baseline VSD signal from bulk-stained samples is often high relative to the change. In other words, there are many membrane components that do not respond to stimulation but are stained with VSD. The use of our confocal microscope module did not resolve this issue, as shown in Fig. 4. However, recent progress in the development of a voltage-sensitive fluorescent protein (Akemann et al. 2010, 2012; Baker et al. 2008; Knöpfel 2008, 2012; Kralj et al. 2011, 2012) may offer a solution, as the combination of this technique with our confocal module should produce clearer signals.

As is shown in Figs. 4 and 5, our new confocal microscope is capable of VSD and Ca^{2+} imaging at very fast acquisition rates while maintaining a high SNR and should have applications for use with new imaging techniques where the high frame rate and low noise are needed.

ACKNOWLEDGMENTS

We thank Dr. Michinori Ichikawa of BrainVision Inc. for sharing the idea of the confocal microscope and Yoshiharu Saitoh of Olympus Engineering for building the confocal unit.

GRANTS

This study was supported by Ministry of Health, Labour and Welfare (Grants H20-Kagaku-Ippan-009 and H23-Kagaku-Ippan-004), JST A-STEP, and Kakenhi (Grants 24500269 and 24240076).

DISCLOSURES

There are no conflicts of interest, financial or otherwise, to declare by the author(s).

AUTHOR CONTRIBUTIONS

T.T. and Y.T. conception and design of research; T.T. designed the optics; Y.T. developed the software; T.T. and Y.T. performed experiments; T.T. and Y.T. analyzed data; T.T. and Y.T. interpreted results of experiments; T.T. and Y.T. prepared figures; T.T. and Y.T. drafted manuscript; T.T. and Y.T. edited and revised manuscript; T.T. and Y.T. approved final version of manuscript.

REFERENCES

Akemann W, Mutoh H, Perron A, Park YK, Iwamoto Y, Knöpfel T. Imaging neural circuit dynamics with a voltage-sensitive fluorescent protein. *J Neurophysiol* 108: 2323–2337, 2012.

Akemann W, Mutoh H, Perron A, Rossier J, Knöpfel T. Imaging brain electric signals with genetically targeted voltage-sensitive fluorescent proteins. *Nat Methods* 7: 643–649, 2010.

Amos WB, White JG. How the confocal laser scanning microscope entered biological research. *Biol Cell* 95: 335–342, 2003.

Baker BJ, Mutoh H, Dimitrov D, Akemann W, Perron A, Iwamoto Y, Jin L, Cohen LB, Isacoff EY, Pieribone VA, Hughes T, Knöpfel T. Genetically encoded fluorescent sensors of membrane potential. *Brain Cell Biol* 36: 53–67, 2008.

Barkat TR, Polley DB, Hensch TK. A critical period for auditory thalamocortical connectivity. *Nat Neurosci* 14: 1189–1194, 2011.

Bradley J, Luo R, Otis TS, DiGregorio DA. Submillisecond optical reporting of membrane potential in situ using a neuronal tracer dye. *J Neurosci* 29: 9197–9209, 2009.

Brakenhoff GJ, Blom P, Barends P. Confocal scanning light microscopy with high aperture immersion lenses. *J Microsc* 117: 219–232, 2011.

Bullen A, Patel SS, Saggau P. High-speed, random-access fluorescence microscopy: I. High-resolution optical recording with voltage-sensitive dyes and ion indicators. *Biophys J* 73: 477–491, 1997.

Bullen A, Saggau P. High-speed, random-access fluorescence microscopy: II. Fast quantitative measurements with voltage-sensitive dyes. *Biophys J* 76: 2272–2287, 1999.

Cohen LB, Salzberg BM, Davila HV, Ross WN, Landowne D, Waggoner AS, Wang CH. Changes in axon fluorescence during activity: molecular probes of membrane potential. *J Membr Biol* 19: 1–36, 1974.

Cohen LB, Salzberg BM, Grinvald A. Optical methods for monitoring neuron activity. *Annu Rev Neurosci* 1: 171–182, 1978.

DiFranco M, Quinonez M, Vergara JL. The delayed rectifier potassium conductance in the sarcolemma and the transverse tubular system membranes of mammalian skeletal muscle fibers. *J Gen Physiol* 140: 109–137, 2012.

DiGregorio DA, Peskoff A, Vergara JL. Measurement of action potential-induced presynaptic calcium domains at a cultured neuromuscular junction. *J Neurosci* 19: 7846–7859, 1999.

Dombeck DA, Blanchard-Desce M, Webb WW. Optical recording of action potentials with second-harmonic generation microscopy. *J Neurosci* 24: 999–1003, 2004.

Dombeck DA, Sacconi L, Blanchard-Desce M, Webb WW. Optical recording of fast neuronal membrane potential transients in acute mammalian brain slices by second-harmonic generation microscopy. *J Neurophysiol* 94: 3628–3636, 2005.

Duemani Reddy G, Kelleher K, Fink R, Saggau P. Three-dimensional random access multiphoton microscopy for functional imaging of neuronal activity. *Nat Neurosci* 11: 713–720, 2008.

Escobar AL, Monck JR, Fernandez JM, Vergara JL. Localization of the site of Ca^{2+} release at the level of a single sarcomere in skeletal muscle fibres. *Nature* 367: 739–741, 1994.

Fink AE, Bender KJ, Trussell LO, Otis TS, DiGregorio DA. Two-photon compatibility and single-voxel, single-trial detection of subthreshold neuronal activity by a two-component optical voltage sensor. *PLoS One* 7: e41434, 2012.

Friedrich M, Gan Q, Ermolayev V, Harms GS. STED-SPIM: stimulated emission depletion improves sheet illumination microscopy resolution. *Biophys J* 100: L43–L45, 2011.

Goldstein SR, Hubin T, Rosenthal S, Washburn C. A confocal video-rate laser-beam scanning reflected-light microscope with no moving parts. *J Microsc* 157: 29–38, 1990.

Grinvald A, Frostig RD, Lieke E, Hildesheim R. Optical imaging of neuronal activity. *Physiol Rev* 68: 1285–1366, 1988.

Grinvald A, Hildesheim R. VSDI: a new era in functional imaging of cortical dynamics. *Nat Rev Neurosci* 5: 874–885, 2004.

Grinvald A, Manker A, Segal M. Visualization of the spread of electrical activity in rat hippocampal slices by voltage-sensitive optical probes. *J Physiol* 333: 269–291, 1982.

Huisken J. Slicing embryos gently with laser light sheets. *Bioessays* 34: 406–411, 2012.

Huisken J, Stainier DY. Even fluorescence excitation by multidirectional selective plane illumination microscopy (mSPIM). *Opt Lett* 32: 2608–2610, 2007.

Huisken J, Stainier DY. Selective plane illumination microscopy techniques in developmental biology. *Development* 136: 1963–1975, 2009.

Ichikawa M, Iijima T, Matsumoto G. Real-time optical recording of neuronal activities in the brain. In: *Brain Mechanisms of Perception and Memory*, edited by Ono T, Squire LR, Raichle ME, Perett DI, Fukuda M. New York: Oxford Univ. Press, 1993, p. 638–648.

Ikegaya Y, Aaron G, Cossart R, Aronov D, Lampl I, Ferster D, Yuste R. Synfire chains and cortical songs: temporal modules of cortical activity. *Science* 304: 559–564, 2004.

Kino GS. Intermediate optics in Nipkow disk microscopes. In: *Handbook of Biological Confocal Microscopy*, edited by Pawley JB. New York: Plenum Press, 1995, p. 155–165.

Knöpfel T. Expanding the toolbox for remote control of neuronal circuits. *Nat Methods* 5: 293–295, 2008.

Knöpfel T. Genetically encoded optical indicators for the analysis of neuronal circuits. *Nat Rev Neurosci* 13: 687–700, 2012.

Knöpfel T, Díez-García J, Akemann W. Optical probing of neuronal circuit dynamics: genetically encoded versus classical fluorescent sensors. *Trends Neurosci* 29: 160–166, 2006.

Kralj JM, Douglass AD, Hochbaum DR, Maclaurin D, Cohen AE. Optical recording of action potentials in mammalian neurons using a microbial rhodopsin. *Nat Methods* 9: 90–95, 2012.

Kralj JM, Hochbaum DR, Douglass AD, Cohen AE. Electrical spiking in *Escherichia coli* probed with a fluorescent voltage-indicating protein. *Science* 333: 345–348, 2011.

Loew LM, Cohen LB, Dix J, Fluhler EN, Montana V, Salama G, Wu JY. A naphthyl analog of the aminostyryl pyridinium class of potentiometric membrane dyes shows consistent sensitivity in a variety of tissue, cell, and model membrane preparations. *J Membr Biol* 130: 1–10, 1992.

Nishimura M, Shirasawa H, Song WJ. A light-emitting diode light source for imaging of neural activities with voltage-sensitive dyes. *Neurosci Res* 54: 230–234, 2006.

Nuriya M, Jiang J, Nemet B, Eisenthal KB, Yuste R. Imaging membrane potential in dendritic spines. *Proc Natl Acad Sci USA* 103: 786–790, 2006.

Ohki K, Chung S, Ch'ng YH, Kara P, Reid RC. Functional imaging with cellular resolution reveals precise micro-architecture in visual cortex. *Nature* 433: 597–603, 2005.

Otsu Y, Bormuth V, Wong J, Mathieu B, Dugué GP, Feltz A, Dieudonné S. Optical monitoring of neuronal activity at high frame rate with a digital random-access multiphoton (RAMP) microscope. *J Neurosci Methods* 173: 259–270, 2008.

Pawley JB. *Handbook of Biological Confocal Microscopy*. Boston, MA: Springer, 2006.

Peterka DS, Takahashi H, Yuste R. Imaging voltage in neurons. *Neuron* 69: 9–21, 2011.

Peterlin ZA, Kozloski J, Mao BQ, Tsiola A, Yuste R. Optical probing of neuronal circuits with calcium indicators. *Proc Natl Acad Sci USA* 97: 3619–3624, 2000.

Ratzlaff EH, Grinvald A. A tandem-lens epifluorescence macroscope: hundred-fold brightness advantage for wide-field imaging. *J Neurosci Methods* 36: 127–137, 1991.

Saggau P. New methods and uses for fast optical scanning. *Curr Opin Neurobiol* 16: 543–550, 2006.

Saggau P, Bullen A, Patel SS. Acousto-optic random-access laser scanning microscopy: fundamentals and applications to optical recording of neuronal activity. *Cell Mol Biol* 44: 827–846, 1998.

Salzberg BM, Davila HV, Cohen LB. Optical recording of impulses in individual neurons of an invertebrate central nervous system. *Nature* 246: 508–509, 1973.

Suh J, Rivest AJ, Nakashiba T, Tominaga T, Tonegawa S. Entorhinal cortex layer III input to the hippocampus is crucial for temporal association memory. *Science* 334: 1415–1420, 2011.

Tominaga T, Tominaga Y. GABAA receptor-mediated modulation of neuronal activity propagation upon tetanic stimulation in rat hippocampal slices. *Pflügers Arch* 460: 875–889, 2010.

Tominaga T, Tominaga Y, Yamada H, Matsumoto G, Ichikawa M. Quantification of optical signals with electrophysiological signals in neural activities of Di-4-ANEPPS stained rat hippocampal slices. *J Neurosci Methods* 102: 11–23, 2000.

Tominaga Y, Ichikawa M, Tominaga T. Membrane potential response profiles of CA1 pyramidal cells probed with voltage-sensitive dye optical imaging in rat hippocampal slices reveal the impact of GABA(A)-mediated feed-forward inhibition in signal propagation. *Neurosci Res* 64: 152–161, 2009.

Tominaga Y, Tominaga T, Ichikawa M. A newly developed CMOS imager to neuronal activity recording (Program no. 457.3) (Online). In: *2005 Neuroscience Meeting Planner*. Washington, DC: Society for Neuroscience, 2005.

Turaga D, Holy TE. Organization of vomeronasal sensory coding revealed by fast volumetric calcium imaging. *J Neurosci* 32: 1612–1621, 2012.

Vranesic I, Iijima T, Ichikawa M, Matsumoto G, Knöpfel T. Signal transmission in the parallel fiber-Purkinje cell system visualized by high-resolution imaging. *Proc Natl Acad Sci USA* 91: 13014–13017, 1994.

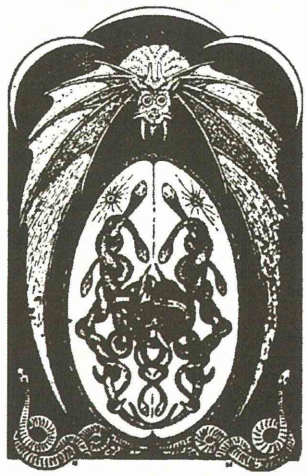

Neuroscience Research 72 (2012) 23–31

Contents lists available at SciVerse ScienceDirect

Neuroscience Research

journal homepage: www.elsevier.com/locate/neures

Induction of superficial cortical layer neurons from mouse embryonic stem cells by valproic acid

Berry Juliandi[a,b], Masahiko Abematsu[a,c], Tsukasa Sanosaka[a], Keita Tsujimura[a], Austin Smith[d,e], Kinichi Nakashima[a,*]

[a] Laboratory of Molecular Neuroscience, Graduate School of Biological Sciences, Nara Institute of Science and Technology, Ikoma, Nara 630-0192, Japan
[b] Department of Biology, Bogor Agricultural University (IPB), Bogor, Indonesia
[c] Department of Orthopaedic Surgery, Graduate School of Medical and Dental Sciences, Kagoshima University, Kagoshima, Japan
[d] Wellcome Trust Centre for Stem Cell Research, University of Cambridge, Cambridge, United Kingdom
[e] Department of Biochemistry, University of Cambridge, Cambridge, United Kingdom

ARTICLE INFO

Article history:
Received 17 August 2011
Received in revised form
13 September 2011
Accepted 29 September 2011
Available online 6 October 2011

Keywords:
Neurogenesis
Corticogenesis
mESCs
HDAC inhibitor
Valproic acid
Histone acetylation

ABSTRACT

Within the developing mammalian cortex, neural progenitors first generate deep-layer neurons and subsequently more superficial-layer neurons, in an inside-out manner. It has been reported recently that mouse embryonic stem cells (mESCs) can, to some extent, recapitulate cortical development *in vitro*, with the sequential appearance of neurogenesis markers resembling that in the developing cortex. However, mESCs can only recapitulate early corticogenesis; superficial-layer neurons, which are normally produced in later developmental periods *in vivo*, are under-represented. This failure of mESCs to reproduce later corticogenesis *in vitro* implies the existence of crucial factor(s) that are absent or uninduced in existing culture systems. Here we show that mESCs can give rise to superficial-layer neurons efficiently when treated with valproic acid (VPA), a histone deacetylase inhibitor. VPA treatment increased the production of Cux1-positive superficial-layer neurons, and decreased that of Ctip2-positive deep-layer neurons. These results shed new light on the mechanisms of later corticogenesis.

1. Introduction

The mammalian cerebral cortex displays a complex structure with a high diversity of neuronal subtypes (Molyneaux et al., 2007). Within this structure, approximately 80% of the neurons are pyramidal excitatory cells which are derived from radial glial progenitors in the ventricular zone (VZ), and are generated in a well defined spatio-temporal manner (Guillemot et al., 2006; Leone et al., 2008). The first neurons generated are Cajal-Retzius cells, which will reside in the most superficial cortical layer (layer I). Subsequent neurogenesis proceeds in an inside-out fashion, by producing deep-layer neurons (layers V and VI) and then progressively more superficial-layer neurons (layers II–IV).

We have devised an adherent monolayer culture of mouse embryonic stem cells (mESCs) for the efficient generation of neuroectodermal precursors and neural stem cells (Ying et al., 2003; Conti et al., 2005). This system reduces the limitation and complexity of neural induction that are characteristic of multicellular aggregation (Bain et al., 1995; Wiles and Johansson, 1999) and/or co-culture methods (Kawasaki et al., 2000), and permits direct observation and manipulation of the cells under study. Recently, a better understanding of cortical neurogenesis was attained using our monolayer culture system. Gaspard et al. (2008) showed that, in the presence of sonic hedgehog (Shh) inhibitor, mESCs generate cortical neurons in a sequential fashion similar to that observed in the developing cortex. Despite this breakthrough result, the experiment failed to completely recapitulate later aspects of cortical development. Gaspard et al. (2008) had better success in generating early-born or deep-layer neurons than in generating superficial-layer neurons. Earlier, Shen et al. (2006) also reported that fewer superficial-layer neurons than deep-layer neurons were generated when they cultured cortical neural stem cells isolated at different gestational time points. This inefficiency in reproducing later events of cortical neurogenesis *in vitro* implies the existence of crucial factors which are not present or induced in current experimental systems.

Epigenetic mechanisms such as DNA methylation and histone modification including acetylation are now known to be critical intrinsic programs that dictate fate specification and differentiation of stem cells. Histone acetylation and deacetylation are mediated by histone acetyltransferases (HATs) and histone deacetylases (HDACs), respectively. In general, an increase of histone acetylation

* Corresponding author. Tel.: +81 743 72 5471; fax: +81 743 72 5479.
E-mail address: kin@bs.naist.jp (K. Nakashima).

0168-0102/$ – see front matter © 2011 Elsevier Ireland Ltd and the Japan Neuroscience Society. All rights reserved.
doi:10.1016/j.neures.2011.09.012

© 2014. Published by The Company of Biologists Ltd | Development (2014) 141, 761-772 doi:10.1242/dev.095802

RESEARCH ARTICLE

STEM CELLS AND REGENERATION

Foxa2 acts as a co-activator potentiating expression of the Nurr1-induced DA phenotype via epigenetic regulation

Sang-Hoon Yi[1,2,‡], Xi-Biao He[1,2,‡], Yong-Hee Rhee[1,2,3], Chang-Hwan Park[2,3], Takumi Takizawa[4,*], Kinichi Nakashima[4] and Sang-Hun Lee[1,2,§]

ABSTRACT

Understanding how dopamine (DA) phenotypes are acquired in midbrain DA (mDA) neuron development is important for bioassays and cell replacement therapy for mDA neuron-associated disorders. Here, we demonstrate a feed-forward mechanism of mDA neuron development involving Nurr1 and Foxa2. Nurr1 acts as a transcription factor for DA phenotype gene expression. However, Nurr1-mediated DA gene expression was inactivated by forming a protein complex with CoREST, and then recruiting histone deacetylase 1 (Hdac1), an enzyme catalyzing histone deacetylation, to DA gene promoters. Co-expression of Nurr1 and Foxa2 was established in mDA neuron precursor cells by a positive cross-regulatory loop. In the presence of Foxa2, the Nurr1-CoREST interaction was diminished (by competitive formation of the Nurr1-Foxa2 activator complex), and CoREST-Hdac1 proteins were less enriched in DA gene promoters. Consequently, histone 3 acetylation (H3Ac), which is responsible for open chromatin structures, was strikingly increased at DA phenotype gene promoters. These data establish the interplay of Nurr1 and Foxa2 as the crucial determinant for DA phenotype acquisition during mDA neuron development.

KEY WORDS: Foxa2, Nurr1, Midbrain dopamine neuron, Development, Neural precursor cell, Epigenetic control, CoREST, Hdac, Mouse

INTRODUCTION

Midbrain dopamine (mDA) neurons play important roles in voluntary movement, emotion and reward-based behaviors. Dysfunction or degeneration of this neuronal subtype is related to major neuropsychiatric disorders such as Parkinson's disease (PD), schizophrenia and drug addiction. Owing to the pathophysiological implications, mDA neurons are the most extensively studied cells. A molecular understanding of mDA neuron development is of high clinical interest as replacing this cell population in diseased brains is considered to be one of the most promising therapeutic approaches for PD (Deierborg et al., 2008; Morizane et al., 2008). In addition, developmental information can be exploited to establish optimal bioassays for mDA neuron-related disorders.

[1]Department of Biochemistry and Molecular Biology, College of Medicine, Hanyang University, Seoul 133-791, Korea. [2]Hanyang Biomedical Research Institute, Hanyang University, Seoul 133-791, Korea. [3]Graduate School of Biomedical Science and Engineering, Hanyang University, Seoul 133-791, Korea. [4]Laboratory of Molecular Neuroscience, Graduate School of Biological Sciences, Nara Institute of Science and Technology, Ikoma, Nara 630-0192, Japan. *Present address: Department of Pediatrics, Graduate School of Medicine, Gunma University, 3-39-22 Showa-machi, Maebashi, Gunma 371-8511, Japan. ‡These authors contributed equally to this work

§Author for correspondence (leesh@hanyang.ac.kr)

Received 22 February 2013; Accepted 9 December 2013

mDA neurons arise from floor plate cells at the ventral midline of the embryonic midbrain (Bonilla et al., 2008; Ono et al., 2007). Sonic hedgehog (Shh), secreted initially by the notochord and later by floor plate cells, induces expression of forkhead family of winged-helix transcription factor 2 (Foxa2; also known as hepatocyte nuclear factor 3 beta), in the midbrain floor plate cells [mouse embryonic day (E) 8.5] (Ang et al., 1993; Monaghan et al., 1993; Placzek, 1995; Sasaki and Hogan, 1994; Sasaki et al., 1997). Foxa2 acts as a master regulator to induce expression of developmental factors specifying mDA neuron precursors such as Nurr1, Pitx3, Lmx1a, Msx1, neurogenin 2 and Mash1 (Ascl1 – Mouse Genome Informatics) (Ang, 2009; Ferri et al., 2007; Kittappa et al., 2007; Lee et al., 2010; Metzakopian et al., 2012). The early inductive role of Foxa2 is probably achieved by cooperation with the Wnt-Lmx1a/b regulatory loop from the isthmic organizer (Chung et al., 2009; Nakatani et al., 2010). The mDA neuron precursors equipped with a battery of developmental factors finally differentiate into mDA neurons during the late stages of ventral midbrain (VM) development.

Nurr1 (Nr4a2 – Mouse Genome Informatics) is an orphan nuclear receptor expressed in late mDA neuron precursors (Saucedo-Cardenas et al., 1998; Zetterström et al., 1996). Mice lacking Nurr1 lack DA phenotype gene expression in the midbrain (Le et al., 1999; Saucedo-Cardenas et al., 1998; Zetterström et al., 1997). Nurr1 has been reported to act as a transcription factor for expression of tyrosine hydroxylase (Th), the rate-limiting enzyme for DA synthesis (Sakurada et al., 1999). Gain-of-function studies have demonstrated that forced Nurr1 expression induces complete DA phenotype gene expression in naive, non-dopaminergic neural precursor cells (NPCs) (Kim et al., 2003a; Shim et al., 2007; Wagner et al., 1999). Thus, Nurr1 is regarded as the most crucial factor in acquiring the DA phenotype during late mDA neuron development. However, Nurr1 expression alone frequently fails to induce the DA phenotype in NPCs (Jin et al., 2006; Lee et al., 2010; Park et al., 2008). In addition, controlled Nurr1 expression at levels and timing similar to physiological levels and timing in the developing midbrain inefficiently induces DA phenotype gene expression (Park et al., 2012). These findings, combined with common properties of nuclear hormone receptor proteins, which are regulated by co-activators and co-inhibitors (Aranda and Pascual, 2001; Purcell et al., 2011; Xu et al., 1999), indicate that the Nurr1-induced DA phenotype expression may require other proteins in the developing VM. Several co-activators have been reported to cooperate with Nurr1 in mDA neuron development (Jacobs et al., 2009b; Lee et al., 2010; Martinat et al., 2006).

Foxa2 expression continues in late mDA precursors and neurons, suggesting that it plays a role in late developmental stages, but how Foxa2 functions in late mDA neuron development is unknown. In this study, we demonstrate that Foxa2 colocalizes with Nurr1 in mDA neuron precursors and acts as a potent co-activator in Nurr1-